Unusual Landau levels in biased bilayer Bernal graphene

Yen-Hung Ho,[1,2,*] Sing-Jyun Tsai,[3,†] Ming-Fa Lin,[3,‡] and Wu-Pei Su[1,§]

[1]*Department of Physics and Texas Center for Superconductivity, University of Houston, Houston, Texas 77204, USA*

[2]*National Center for Theoretical Sciences, National Cheng Kung University, Tainan 701, Taiwan*

[3]*Department of Physics, National Cheng Kung University, Tainan 701, Taiwan*

(Received 20 August 2012; revised manuscript received 21 November 2012; published 13 February 2013)

A generalized tight-binding model is employed to study how electrostatic gating influences the magnetoelectronic properties of a Bernal graphene bilayer. With the availability of the Landau wave function, the distribution among its sublattices enables detailed characterization of the Landau levels as well as their optical responses. The different electric potentials on respective layers break the interlayer symmetry, which in turn lifts the intervalley degeneracy. In addition, Landau levels in response to the bias field make direct crossings and anticrossings. The latter are manifestations of the noncrossing theorem: two states not distinguished by unique quantum numbers perform anticrossing with their wave function characteristics interchanged and strongly mixed near the point of anticrossing. Those significant changes are directly reflected in the magneto-optical spectra, including the splitting of absorption peaks and their enhancement or extinction in response to bias strength.

DOI: 10.1103/PhysRevB.87.075417 PACS number(s): 71.70.Di, 71.15.Ap, 78.20.Ls

Graphene layers have attracted great attention in recent years, mainly owing to their extraordinary electronic properties. The surface charge carriers exhibit extremely high mobility. They can travel ballistically over a submicron distance. This makes graphene layers a promising material for the next-generation electronic devices. However, there are still some existing critical barriers for practical applications. The most important one is the absence of a band gap. For this, several ways have been developed to open a band gap, such as adsorption of hydrogen atoms on the carbon dangling bonds[1] and cutting a graphene sheet into one-dimensional (1D) ribbons with a finite width.[2,3] In particular, the most controllable way is applying a bias electric field on the top and bottom layer of a graphene bilayer. In this way, one can easily modulate the doping level in addition to creating an energy gap.[4–6] In this work, we mainly focus on the coupled bilayer to see how an electrostatic field manipulates the magnetically quantized states as well as their optical responses.

Because of the highly symmetric crystal structure, graphene exhibits multiple degeneracies in its electronic states, such as the electron-hole symmetry and the intervalley symmetry. The latter concerns the similarity of states in the vicinity of K and K' points of the Brillouin zone. Carriers in those two valleys have opposite chiralities similar to spin-1/2 particles. Moreover, graphene is one of the most ideal 2D electronic systems. A perpendicular magnetic field forces the charge carriers to circulate in cyclotron orbits. The planar electronic states are therefore quantized into well-resolved Landau levels, which is beneficial for studying the quantum Hall effects.[7–17] In few-layers, the introduction of an additional bias electric field enables a selective control of charge carriers in each layer, which can lift the intervalley degeneracy and lead to the Landau-level couplings—two states perform an anticrossing with their wave functions strongly hybridized. Such a peculiar feature is absent in standard 2D systems.

The bilayer Bernal graphene is a coupled bilayer with one layer shifted along the armchair direction by the C-C bond length (1.42 Å) with respect to the other layer, as illustrated in Fig. 1(a). The primitive unit cell contains four carbon atoms (A_1-B_1-A_2-B_2), the inequivalent A and B atoms on top ($l = 1$) and bottom ($l = 2$) layers. Considering $2p_z$ orbitals only, the tight-binding wave function is a linear combination of four atomic bases $|\psi\rangle = c_{A_1}|A_1\rangle + c_{B_1}|B_1\rangle + c_{A_2}|A_2\rangle + c_{B_2}|B_2\rangle$, and the Hamiltonian is a 4×4 Hermitian matrix with its elements given by

$$\langle k_{l'}|H|j_l\rangle = \gamma_s\left(\vec{R}_{j_l},\vec{R}_{k_{l'}}\right)\sum \exp\left[i\vec{k}\cdot\left(\vec{R}_{j_l}-\vec{R}_{k_{l'}}\right)\right]. \quad (1)$$

$\vec{R}_{j_l}(\vec{R}_{k_{l'}})$ stands for the position vector of atom $j(k) = A, B$ on layer $l(l') = 1,2$. $\gamma_s(\vec{R}_{j_l},\vec{R}_{k_{l'}})$ represents the hopping integral between atoms. In our numerical calculations, five atomic interactions are taken into account: one intralayer term ($\gamma_0 = -3.12$ eV) and four interlayer terms ($\gamma_1 = 0.38$ eV, $\gamma_3 = 0.28$ eV, $\gamma_4 = 0.12$ eV, and $\gamma_6 = 0.016$ eV).[18–20] γ_6 is the site energy difference between the $A_{1(2)}$ and $B_{1(2)}$ atoms due to the Bernal stacking.

As the coupled bilayer is subjected to a perpendicular magnetic field $B_0\hat{z}$, the vector potential $\vec{A} = (0, B_0x, 0)$ changes the phase of Eq. (1) by a Peierls phase $\Delta G(\vec{R}_{j_l},\vec{R}_{k_{l'}}) = \int_0^1(\vec{R}_{k_{l'}} - \vec{R}_{j_l})\cdot\vec{A}[\vec{R}_{j_l} + \lambda(\vec{R}_{k_{l'}} - \vec{R}_{j_l})]d\lambda$.[20–25] The new matrix element is now expressed as

$$\langle k_{l'}|H|j_l\rangle = \gamma_s\left(\vec{R}_{j_l},\vec{R}_{k_{l'}}\right)\sum \exp\left[i\vec{k}\cdot\left(\vec{R}_{j_l}-\vec{R}_{k_{l'}}\right) + i\frac{e}{\hbar}\Delta G\left(\vec{R}_{j_l},\vec{R}_{k_{l'}}\right)\right]. \quad (2)$$

The Peierls phase serves as another spatially periodic function, which makes the unit cell $2(79\,000/B_0)$ times larger. A magnetic field of 8 T is used throughout this paper. The unit cell is thus extended to a rectangular parallelepiped of 4206.75 nm in length, containing 79000 atoms. The Hamiltonian is therefore a $79\,000 \times 79\,000$ matrix, and the wave function is spanned by 79 000 bases, which can be further divided into groups associated with the four sublattices: $A_{1,i}$, $B_{1,i}$, $A_{2,i}$, $B_{2,i}$ with $i = 1 \sim (79\,000/8)$. The dual gating further induces electrostatic potentials ($+V_g$ and $-V_g$) on respective layers, giving rise to a change of site energy in the diagonal matrix elements of the Hamiltonian. Both the eigenenergies and eigenfunctions are obtained by using an exact diagonalization method,[20–23] which treats all atomic hoppings

 ©2013 American Physical Society

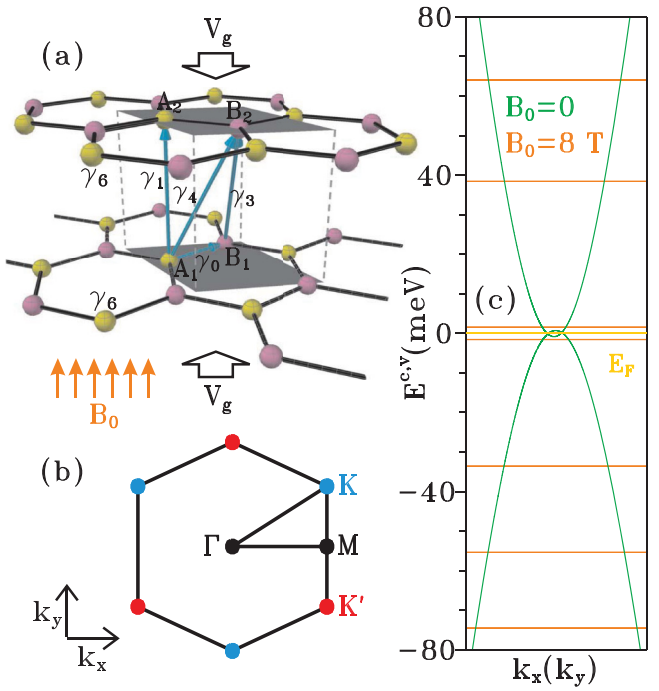

FIG. 1. (Color online) (a) Geometric configuration of bilayer Bernal graphene and (b) the associated reciprocal space. (c) Low-energy electronic structures at zero field (green curves) and quantized Landau levels at a magnetic field of 8 T (orange curves).

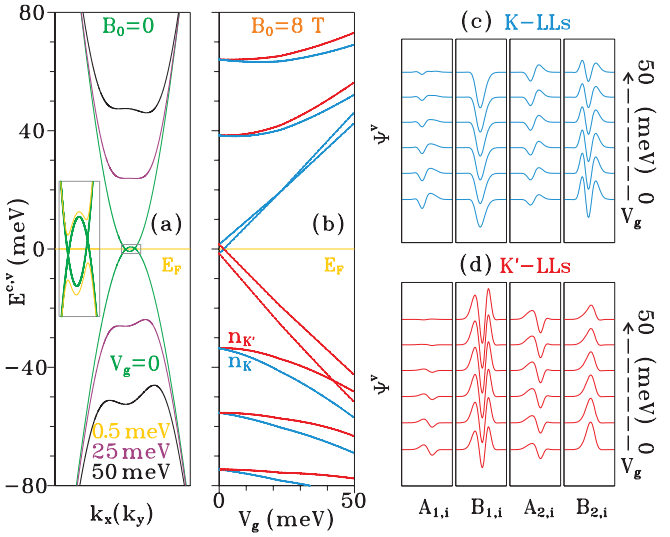

FIG. 2. (Color online) (a) Low-energy bands at zero magnetic field but at different bias electric fields V_g. (b) The Landau-level energies at $B_0 = 8$ T in response to V_g. The Landau wave functions in the four constituent sublattices for occupied (c) $n_K = 2$ and (d) $n_{K'} = 2$ states. From bottom to top are at V_g from 0 to 50 meV. The width of the horizontal axis is 1425 nm centered at 1/6 of the extended unit cell for (c) K states, and at 2/6 for (d) K' states.

(γ_i; $i = 0,1,3,4,6$), magnetic field (B_0) and bias field (V_g) on the same footing, without introducing any approximation.

At zero external field, the couplings between layers change the linear dispersion of the monolayer into parabolic bands, as shown by the green curves in Fig. 1(c). The valence and conduction bands are asymmetric with respect to the Fermi level $E_F = 0$, and they slightly overlap near E_F, which makes this system behave like a semimetal. In a perpendicular magnetic field $\mathbf{B} = B_0\hat{z}$, the planar electrons are fully quantized into dispersionless Landau levels (orange curves). The low-lying levels exhibit linear field dependence $E^{c,v} \propto \sqrt{n^{c,v}(n^{c,v}+1)}B_0$.[20–22] $n^{c,v}$ is a quantum number characterizing individual Landau states. Its value can be directly determined from the wave functions defined on the sublattices.[20–25]

A Landau wave function can best be described by its behavior on the four sublattices ($A_{1,i}$-$B_{1,i}$-$A_{2,i}$-$B_{2,i}$). Each Landau level is fourfold degenerate, and in the gauge chosen the wave functions are respectively localized near 1/6, 2/6, 4/6, 5/6 of the extended unit cell. In particular, the 1/6 (2/6) states, similar to the 5/6 (4/6) ones, actually correspond to states near valley K (K'). As illustrated in Figs. 2(c) and 2(d), respectively, for K and K' states, each wave function consists of four sublattice components resembling the Hermite polynomials with node number n. This is the usual wave function of the Landau states in the Cartesian coordinate representation. The relationship of the node numbers associated with the sublattices is $A_{1,i}$:$B_{1,i}$:$A_{2,i}$:$B_{2,i}$ = $n-1$:$n-2$:$n-1$:n for K-valley states and $n-1$:n:$n-1$:$n-2$ for K'-valley states. The node number of $B_{2,i}$ ($B_{1,i}$) is taken to be the level index $n_K^{c,v}$ ($n_{K'}^{c,v}$) of K- (K')-Landau states since $B_{1,i}$ and $B_{2,i}$ sites have evidently stronger weight than $A_{1,i}$ and $A_{2,i}$. The remaining $A_{1,i}$ and $A_{2,i}$ sites gradually gain their weight with increasing state energy. The way the Landau wave function distributes among sublattices, together with the state energy, can be tuned through the electrostatic gating.

Applying a gate voltage causes the two layers to have opposite electric potentials $\pm V_g$, which substantially alters the low-energy bands. As shown in the inset of Fig. 2(a) for $B_0 = 0$, the valence and conduction bands avoid crossing each other as V_g is turned on, an energy gap is thus created for $V_g > 0.2$ meV, which turns the semimetallic bilayer into a semiconductor. An increase in V_g pushes the two bands away from the charge neutral point. The parabolic dispersions take on the sombrero shapes that expand in height (energy) and width (momentum). Each band contains three band edges with the middle one located right at momentum K (K').

The degeneracy of valleys K and K' no longer holds once the transverse electric and magnetic fields are both present. Figure 2(b) illustrates the splitting of K and K' Landau energies in response to V_g. Such level splittings can be physically explained by the value of V_g and the changes of wave functions on the sublattices. Within a perturbation scheme, the energy shift is given by $\langle A_1| - V_g|A_1\rangle + \langle B_1| - V_g|B_1\rangle + \langle A_2|V_g|A_2\rangle + \langle B_2|V_g|B_2\rangle$. At $V_g = 0$, the K and K' states are fully degenerate. For wave functions on the sublattices, those of K and K' states are symmetric in weights at $V_g = 0$, i.e., $|c^K_{A_1(B_1)}| = |c^{K'}_{A_2(B_2)}|$ and $|c^{K'}_{A_1(B_1)}| = |c^K_{A_2(B_2)}|$. However, such a balance is soon lost once V_g is applied, as shown in Figs. 2(c) and 2(d). For both K and K' states, their B_1 and A_2 sites are enhanced in weight while A_1 and B_2 are suppressed. A similar effect can be obtained for the unoccupied states $n^c_{K(K')} \geqslant 2$ but with opposite trend (not shown). Those changes together with the value of V_g enable us to estimate the degree of energy shift between the two valley

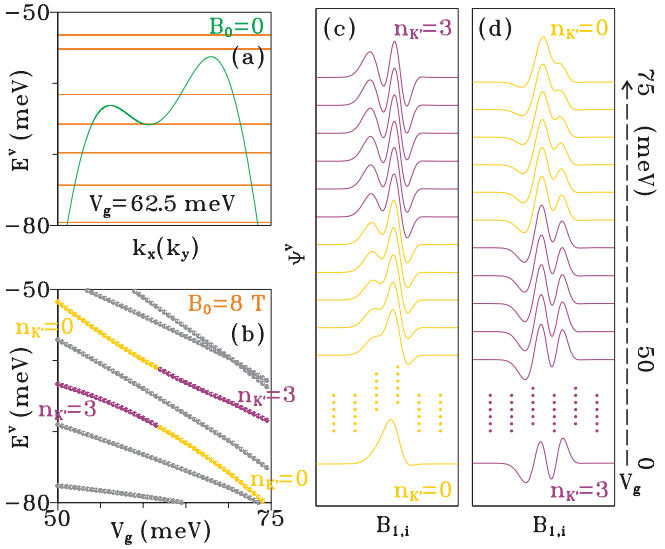

FIG. 3. (Color online) (a) Mexican-hat band profile at $B_0 = 0$ and $V_g = 62.5$ meV. (b) The Landau energies varied with V_g at $B_0 = 8$ T, where the two interacting Landau states are colored purple and yellow. (c)–(d) The V_g-dependent Landau wave function in $B_{1,i}$ sublattice respectively for $n^v_{K'} = 0$ and $n^v_{K'} = 3$ states. From bottom to top are at bias field $V_g = 0$ and from 50 meV to 75 meV. The physical unit of horizontal axis is the same as Fig. 2(d).

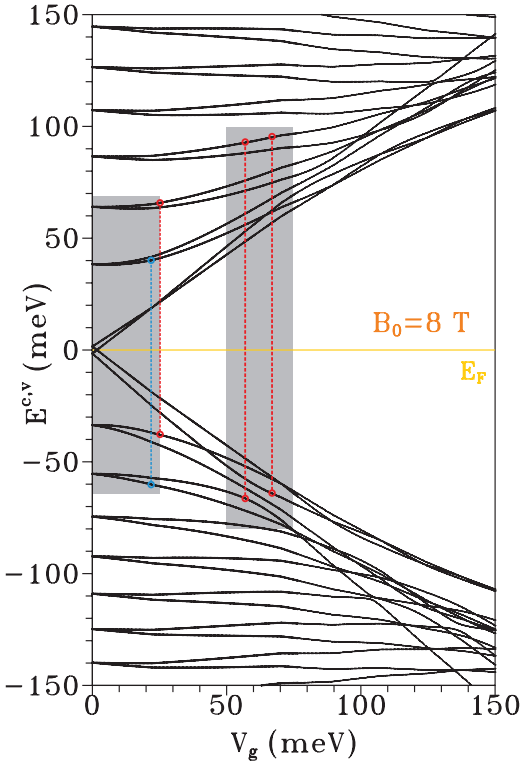

FIG. 4. (Color online) Landau-level energies at $B_0 = 8$ T as a function of bias electric field V_g. The left and right shaded areas cover the Landau levels involving the optical transitions respectively in Figs. 5(a) and 5(b), where the transitions mainly discussed are indicated by dashed lines.

states. Furthermore, the weight changes among sublattices due to V_g also make it possible to estimate the induced charges in respective layers.

Lower Landau levels are more sensitive to electrostatic gating, including the degree of energy shift and the splitting of K and K' states. As the field is strong enough ($V_g >$ 80 meV), those lower levels inevitably intersect other higher levels, which gives rise to a change of filling factor in magnetoresistance.[8,26,27] The way the Landau levels interact is either direct crossing or anticrossing. The latter case is of particular interest and will be discussed next.

The dual gating changes the low-energy bands to the sombrerolike energy dispersions [Fig. 3(a)], which also leads to the Landau-level couplings at nonzero magnetic field [Fig. 3(b)]. In certain field ranges, two V_g-dependent Landau levels effectively repel each other instead of direct penetrations, e.g., the two branches colored purple and yellow in Fig. 3(b). Such anticrossings take place as two levels belong to the same valley, either K or K', and their quantum numbers $n^{c,v}$ differ by integral multiples of three $\Delta n = 3I$. Figure 3(b) illustrates the coupling of $n^v_{K'} = 0$ and $n^v_{K'} = 3$ levels. Also shown in Fig. 4 on a larger scale, such couplings are more evident for smaller I and become more frequent as V_g grows. The γ_1 hopping plays a central role to form the sombrero band profile at $B_0 = 0$ and thus at $B_0 \neq 0$ the multiple level crossings as a function of V_g, while the anticrossings are triggered by the γ_3 hopping, which is also responsible for the trigonal anisotropy in the 2D energy bands at $B_0 = 0$.

The wave function distribution serves as a fingerprint for those Landau-level couplings. As two levels repel each other, they experience radical changes in constituent sublattices. As shown in Figs. 3(c) and 3(d), initially the two states have well-identified oscillation modes on the sublattices. However, as the two levels recede from each other, they interchange their oscillation modes on the same sublattice, which is revealed as the color change in Figs. 3(b)– 3(d). In between, the two modes are strongly hybridized. It is noteworthy that such hybridized states fail to possess well defined quantum number $n^{c,v}$ since they no longer have the well-characterized oscillation modes. For the other direct intersecting cases, on the contrary, no evident change takes place in the Landau wave functions.

In order to understand the physical origin of those anticrossings, we further examined the wave functions in detail and found that, in our numerically calculations at $V_g = 0$, each sublattice is composed of the Hermite polynomial not only the fundamental n mode but also the minor components of $n \pm 3$ modes. This arises from the inclusion of γ_3, which was also qualitatively predicted in the previous effective-mass approximation.[28] The bias potential acting on the diagonal Hamiltonian matrix elements shifts the energy of individual Landau levels. As levels of $n_{K(K')} = n$ and $n'_{K(K')} = n \pm 3$ are brought together in energy, they effectively interact with each other since they are actually not distinguished by unique quantum numbers. The two wave functions contain part of the same oscillation modes, and the Wigner-von Neumann noncrossing rule prohibits states with the same modes from crossing. That is, the major n (minor $n \pm 3$) mode of the $n_{K(K')} = n$ level interacts with the minor n (major $n \pm 3$) mode of the $n'_{K(K')} = n \pm 3$ level with the proximity of state energy. Consequently, the two states avoid crossing each other. In terms of wave functions, they exchange the

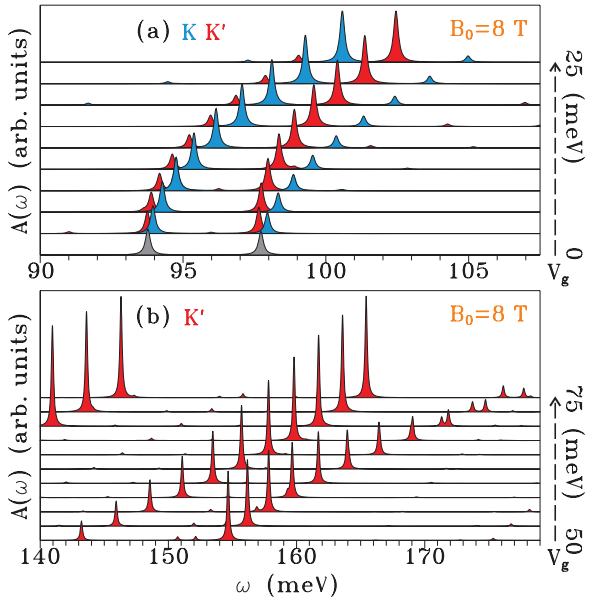

FIG. 5. (Color online) Magneto-optical absorption spectra, which reflect (a) the splitting of K and K' Landau states and (b) the Landau-level anticrossing of occupied K' states. From bottom to top shows the V_g evolution of optical spectra for (a) $V_g = 0 \rightarrow 25$ meV and (b) $50 \rightarrow 75$ meV. The states involved in those transitions are located within the shaded areas in Fig. 4.

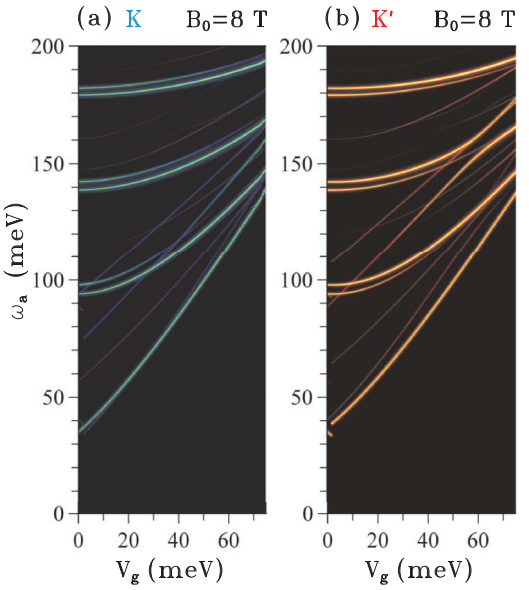

FIG. 6. (Color online) Contour plots of optical spectra as a function of bias strength V_g and photon energy ω_a at $B_0 = 8$ T. Absorption rate from weak to strong reveals as (a) black-blue-green for transitions of K Landau states, and (b) black-red-yellow for those of K'.

characteristic modes, and are strongly mixed near the point of the anticrossing.

Landau wave function is a key element in calculating the magneto-optical spectra. In particular, the numerical solutions of the wave function provide a straightforward way to access the selection rules and absorption rates.[20–25] In the calculation of optical spectra, the interaction between electron and photon are described by the velocity matrix element $\langle\psi|\nabla_k H|\psi'\rangle$. Its main contribution comes from the in-plane hopping term (γ_0) in the Hamiltonian sandwiched between the initial and final wave functions defined on the same layer but on different sublattices, $\langle A_l^{v(c)}|\nabla_k H_{\in\gamma_0}|B_l^{c(v)}\rangle$. For an optical transition to take place, the orthogonality relation of Hermite polynomials demands that the wave function of the occupied state defined on one sublattice must have the same oscillation mode as the wave function of the unoccupied state defined on the other sublattice. That leads to the optical selection rules $\Delta n = \pm 1$ based on the way we assign the level index $n^{c,v}$. The calculated absorption spectra are shown in Fig. 5(a). Those peaks occur in pairs representing transitions the types of $n^v \rightarrow n^c + 1$ and $n^v + 1 \rightarrow n^c$. In each pair, the energy difference comes solely from the electron-hole asymmetry due to interlayer couplings γ_4 and γ_6, which has been verified by experiments.[20–22,29] Those peaks are substantially altered through the electrical gating, which can be understood in terms of the changes in Landau energies and wave functions.

Optical transitions are allowed only between states in the same valley, either K or K'. This is because different valley states have their wave functions localized at quite different positions, either 1/6 or 2/6, the intervalley transitions are therefore strictly forbidden. In Fig. 5(a), the optical spectra of K and K' states are respectively colored blue and red. The two spectra are exactly identical at $V_g = 0$ (colored gray) since the involved Landau states are fully degenerate. Once V_g is applied, the symmetry between K and K' states is broken, which makes the absorption peaks diverge both in position and intensity. In addition to the overall shift to higher energy with increasing V_g, the K spectra is blue shifted while the K' is red shifted with respect to K. Simply speaking, the twin peaks at $V_g = 0$ are split into four peaks. For each pair of the K spectra, the lower-energy peak is enhanced in intensity while the higher-energy one is suppressed. This trend is, however, opposite for the K' spectra. This can be intuitively explained by the weight changes among sublattices in response to the bias field, as described in Figs. 2(c) and 2(d).

The Landau-level anticrossings and mixings caused by tuning V_g also manifest themselves in the optical absorption spectra, as shown in Fig. 5(b). In terms of peak positions against V_g, two prominent peaks head toward each other and pull away afterward. In particular, the lower-energy channel gradually grows in intensity as the V_g value enters the mixing region, and it ends up with a strong peak beyond this region. On the contrary, the other channel with higher energy begins with a pronounced peak and ends up with a weak one. For these peaks, the strengthening and weakening in intensity can be ascribed to the changes in wave functions, as mentioned in connection with Figs. 3(c) and 3(d). It should be also noted that there exist other minor peaks with selection rules $\Delta n = 4, 7, 10, \ldots$, in which their intensities can serve as another fingerprint for the degree of Landau-level couplings in virtue of the mixings of wave functions. In fact, for those transitions involving the anticrossing states, they cease to have well-characterized selection rules. Figure 6 shows the contour plot of spectra with a wider range of photon energy and bias strength, providing a clearer identification of the anomalies found in this work. The symmetry breaking of K and K' valley states is observable by

comparing Figs. 6(a) and 6(b). Tracing those absorption lines also allows one to point out the level crossing and anticrossing, as well as their enhancement or extinction in response to V_g.

Whether the two valley levels split and whether the level anticrossings appear intimately depends on the stacking sequence and layer numbers. (a) To make the opposite valley states split, the asymmetry between top and bottom layers is required. For instance, the AA bilayer and ABA trilayer keep the inversion symmetry, so they fail to lift the valley degeneracy by tuning the interlayer potential. (b) The stacking order dominates the low-energy bands and thus the appearance of level anticrossings.[25,30–33] Except for the AA-stacked ones, other multilayers are expected to have parabolic bands close to the Fermi level. An external gating can easily convert them into sombrerolike dispersions. As a result, the level anticrossings are in general available in most coupled multilayer systems. However, the extent of those Landau-level couplings still relies on the stacking manner. For example, in biased trilayer systems at $B_0 = 0$, it is much easier to form the sombrero band profile in ABC stacking than in ABA one. Therefore, the former is more promising to observe those Landau-level couplings.

In summary, we have predicted the following remarkable phenomena in graphene bilayer: electrostatic gating effectively lifts the intervalley degeneracy and gives rise to Landau-level couplings. A close inspection of Landau wave functions provides a physical understanding of those results. All of those have their direct counterparts in the magneto-optical spectra, including the peak positions and peak intensities, which can be verified by future experiments.

ACKNOWLEDGMENTS

This work was supported by the National Science Council and the National Center for Theoretical Sciences of Taiwan, under Grant No. NSC 98-2112-M-006-013-MY4. Y.H.H. and W.P.S. were partially supported by the Texas Center for Superconductivity and the Robert A. Welch Foundation under Grant No. E-1070.

*yenhungho@gmail.com
†l2894114@mail.ncku.edu.tw
‡mflin@mail.ncku.edu.tw
§wpsu@uh.edu

[1] D. K. Samarakoon and X.-Q. Wang, ACS Nano **4**, 4126 (2010).
[2] V. Barone, O. Hod, and G. E. Scuseria, Nano Lett. **6**, 2748 (2006).
[3] H. C. Chung, M. H. Lee, C. P. Chang, and M. F. Lin, Opt. Express **19**, 23350 (2011).
[4] T. Ohta, A. Bostwick, T. Seyller, K. Horn, and E. Rotenberg, Science **313**, 951 (2006).
[5] C. L. Lu, C. P. Chang, Y. C. Huang, R. B. Chen, and M. L. Lin, Phys. Rev. B **73**, 144427 (2006).
[6] A. B. Kuzmenko, I. Crassee, D. van der Marel, P. Blake, and K. S. Novoselov, Phys. Rev. B **80**, 165406 (2009).
[7] V. Lukose, R. Shankar, and G. Baskaran, Phys. Rev. Lett. **98**, 116802 (2007).
[8] E. V. Castro, K. S. Novoselov, S. V. Morozov, N. M. R. Peres, J. M. B. Lopes dos Santos, J. Nilsson, F. Guinea, A. K. Geim, and A. H. Castro Neto, Phys. Rev. Lett. **99**, 216802 (2007).
[9] D. S. L. Abergel and T. Chakraborty, Phys. Rev. Lett. **102**, 056807 (2009).
[10] M. Nakamura, E. V. Castro, and B. Dora, Phys. Rev. Lett. **103**, 266804 (2009).
[11] V. M. Apalkov and T. Chakraborty, Phys. Rev. Lett. **105**, 036801 (2010).
[12] J. M. Pereira, Jr., F. M. Peeters, and P. Vasilopoulos, Phys. Rev. B **76**, 115419 (2007).
[13] C. Toke and V. I. Fal'ko, Phys. Rev. B **83**, 115455 (2011).
[14] N. A. Goncharuk and L. Smrcka, New J. Phys. **12**, 083048 (2010).
[15] D. L. Wang and G. J. Jin, Europhys. Lett. **92**, 57008 (2010).
[16] M. Mucha-Kruczynski, D. S. L. Abergel, E. McCann, and V. I. Fal'ko, J. Phys.: Condens. Matter **21**, 344206 (2009).
[17] M. Mucha-Kruczyski, E. McCann, and V. I. Fal'ko, Solid State Commun. **149**, 1111 (2009).
[18] K. Nakao, J. Phys. Soc. Jpn. **40**, 761 (1976).
[19] B. Partoens and F. M. Peeters, Phys. Rev. B **74**, 075404 (2006).
[20] Y. H. Ho, Y. H. Chiu, J. Y. Wu, J. Wang, and M. F. Lin, Thil. Trans. R. Soc. A **368**, 5445 (2010).
[21] Y. H. Lai, J. H. Ho, C. P. Chang, and M. F. Lin, Phys. Rev. B **77**, 085426 (2008).
[22] Y. H. Ho, Y. H. Chiu, D. H. Lin, C. P. Chang, and M. F. Lin, ACS Nano **4**, 1465 (2010).
[23] J. Wang, Y. H. Chiu, Y. H. Ho, T. S. Li, and M. F. Lin, Solid State Commun. **151**, 1410 (2011).
[24] Y. H. Ho, J. Wang, Y. H. Chiu, M. F. Lin, and W. P. Su, Phys. Rev. B **83**, 121201(R) (2011).
[25] Y. H. Ho, J. Y. Wu, R. B. Chen, Y. H. Chiu, and M. F. Lin, Appl. Phys. Lett. **97**, 101905 (2010).
[26] R. T. Weitz, M. T. Allen, B. E. Feldman, J. Martin, and A. Yacoby, Science **330**, 812 (2010).
[27] J. Velasco, Jr., L. Jung, W. Bao, Y. Lee, P. Kratz, V. Aji, M. Bockrath, C. N. Lau, C. Varma, R. Stillwell, D. Smirnov, F. Zhang, J. Jung, and A. H. MacDonald, Nature Nanotechnol. **7**, 156 (2012).
[28] M. Inoue, J. Phys. Soc. Jpn. **17**, 808 (1962).
[29] E. A. Henriksen, Z. Jiang, L.-C. Tung, M. E. Schwartz, M. Takita, Y.-J. Wang, P. Kim, and H. L. Stormer, Phys. Rev. Lett. **100**, 087403 (2008).
[30] C. H. Lui, Z. Li, K. F. Mak, E. Cappelluti, and T. F. Heinz, Nature Phys. **7**, 944 (2011).
[31] S. Yuan, R. Roldan, and M. I. Katsnelson, Phys. Rev. B **84**, 125455 (2011).
[32] S. H. Jhang, M. F. Craciun, S. Schmidmeier, S. Tokumitsu, S. Russo, M. Yamamoto, Y. Skourski, J. Wosnitza, S. Tarucha, J. Eroms, and C. Strunk, Phys. Rev. B **84**, 161408(R) (2011).
[33] S. H. R. Sena, J. M. Pereira, Jr., F. M. Peeters, and G. A. Farias, Phys. Rev. B **84**, 205448 (2011).